frontiers in Materials

ORIGINAL RESEARCH
published: 23 March 2021
doi: 10.3389/fmats.2021.649411

N,Cu-CD-Decorated Mesoporous WO_3 for Enhanced Photocatalysis Under UV–Vis–NIR Light Irradiation

Tianjun Ni[1,2], Qiansheng Li[2], Yunhui Yan[2], Zhijun Yang[2], Kaiwen Chang[2] and Guoguang Liu[1,3]**

[1]Henan Key Laboratory for Environmental Pollution Control, Key Laboratory for Yellow River and Huaihe River Water Environment and Pollution Control, Ministry of Education, School of Environment, Henan Normal University, Xinxiang, China, [2]School of Basic Medical Science, Xinxiang Medical University, Xinxiang, China, [3]Faculty of Environmental Science and Engineering, Guangdong University of Technology, Guangzhou, China

Research on the design of semiconductor photocatalysts with rapid electron transfer efficiencies and broad-spectrum responses for environmental remediation remains a pressing challenge. Herein, we described the fabrication of a novel broad-spectrum nitrogen and copper codoped carbon dots/mesoporous WO_3 nanocomposite (N,Cu-CDs/m-WO_3), which exhibited complete UV–vis–NIR spectrum response, light harvesting capabilities, rich oxygen vacancies, rapid electron-transfer ability, low electron–hole (e^-/h^+) pair recombination rate, and extensive specific surface area. After 2 h of photocatalytic reaction, it showed excellent photoactivities for the degradation of rhodamine B, methylene blue, tetracycline hydrochloride, oxytetracycline, ciprofloxacin, and bisphenol A. Moreover, we found that the conversion between Cu (II) and Cu (I) played a key role in accelerating electron transfer and inhibiting the recombination of e^-/h^+ pairs. This work provides an efficient strategy for the utilization of solar light and enhancing the charge-transfer capacity in the semiconductor photocatalysis field.

Keywords: photocatalysis, mesoporous WO_3, N Cu-CDs, full-spectrum response, rapid electron transfer, N Cu-CD/m-WO_3-0.8

OPEN ACCESS

Edited by:
Wei Qin,
Changsha University of Science and Technology, China

Reviewed by:
Dong Yan,
Singapore University of Technology and Design, Singapore
Chao Xia,
Shenzhen University, China

****Correspondence:***
Tianjun Ni
tjni@xxmu.edu.cn
Guoguang Liu
liugg615@163.com

Specialty section:
This article was submitted to Energy Materials, a section of the journal Frontiers in Materials

Received: *04 January 2021*
Accepted: *25 January 2021*
Published: *23 March 2021*

Citation:
Ni T, Li Q, Yan Y, Yang Z, Chang K and Liu G (2021) N,Cu-CD-Decorated Mesoporous WO_3 for Enhanced Photocatalysis Under UV–Vis–NIR Light Irradiation. Front. Mater. 8:649411. doi: 10.3389/fmats.2021.649411

INTRODUCTION

As a novel solar-driven technology, semiconductor photocatalysis for environmental remediation has garnered increasing attention due to its ecogreenness, recyclability, and high efficiency (Daneshvar et al., 2007; Ong, 2017). Of the semiconductor materials (e.g., TiO_2, WO_3, and SnO_2) investigated thus far, WO_3 exhibits extraordinary characteristics including nontoxicity, stability, and favorable band gaps (2.6–3.0 eV) (Liu Y. et al., 2012; Carmona et al., 2016). However, several drawbacks such as low visible-light utilization efficiency and the rapid recombination rate of photoinduced e^-/h^+ pairs still limit its applicability (Zhang et al., 2017). Thus, considerable efforts have been devoted to improve its photocatalytic activity. Note that controlling the formation and structure of heterojunction are two strategies for enhancing the photocatalytic performance of WO_3.

Structural modifications can provide special channels for electron transfer and differently exposed surface areas, thus altering the photocatalytic activity of WO_3 (Wang et al., 2018). Compared with traditional nanostructures, mesoporous structures with extensive specific surface areas, uniform and tunable pore sizes, and large pore volumes endow them with additional reactive reaction sites and unique pathways for the diffusion of molecules, which can better interact with guest molecules (Luo et al., 2013; Zhao et al., 2016; Lv et al., 2017). However, pure mesoporous WO_3 is primarily used in

gas sensors, and there are a few studies about single mesoporous WO_3 employed for photocatalysis (Teoh et al., 2003; Li et al., 2010; Zhu et al., 2017; and Zheng et al., 2019). Besides, the intrinsic absorption of WO_3 is restricted to a marginal portion of the visible-light spectrum. Therefore, the synthesis of heterojunction to facilitate the utilization of solar energy is necessary (Zhang et al., 2017; Ni et al., 2020).

Among various composites, carbon dots (CDs) have been widely applied in photocatalysis due to their excellent physicochemical properties including water solubility, nontoxicity, upconversion capacities, and optical absorption, which can facilitate the charge migration, resulting in enhancing their photocatalytic activity (Li et al., 2012; Zhang et al., 2017; Zhang J. et al., 2019). However, the slow electron-transfer/storage capacities and low light-absorption efficiencies of CDs also limit their practical application. Toward the potential resolution of these deficits, heteroatom doping has been considered as an efficient strategy for improving the physicochemical properties of CDs (Barman et al., 2014; Ma Y. et al., 2017; and Wu et al., 2017). In our previous work, we found that doping nitrogen into carbon dots (N-CDs) could enhance their optical absorption in the visible-light region (Wang et al., 2017; Wang et al., 2019; Zhang J. et al., 2019). In addition, metal doping has also been shown to be an effective method for enhancing the electron-transfer properties of CDs (Wu et al., 2015; Xue et al., 2017). Unlike noble metals, copper (Cu) doping has the advantage of low cost, safety, and inclination to coordinate with CDs chemical groups (Zong et al., 2014; Guo et al., 2015; Xu et al., 2015; Zhang et al., 2017; Zhang W. J. et al., 2019). Several studies have reported that Cu can serve as a multielectron redox reaction site, which can accelerate the electron transfer and broaden the optical absorption, thus improving the photocatalytic activity (Irie et al., 2008; Nakajima et al., 2011; and Ma et al., 2018). Therefore, if N and Cu exist simultaneously in CDs that act as electron donors and acceptors, respectively, which could significantly facilitate electron-transfer and light-absorption capacities. Up to now, there have been no reports about N and Cu codoped CD-decorated WO_3 for photocatalytic application.

Herein, we successfully synthesized a series of mesoporous WO_3 via a solvent evaporation-induced self-assembly (EISA) process using diblock or triblock copolymers PEO_x-b-PS_x (PbS) as the templates, respectively. After decorating with N,Cu-CDs, the N,Cu-CDs/m-WO_3 showed high electron-transfer/reservoir capacities and enhanced photocatalytic degradation activities against rhodamine B (RhB), methylene blue (MB), tetracycline hydrochloride (TCH), oxytetracycline (OTC), ciprofloxacin (CIP), and bisphenol A (BPA) under UV, vis, and NIR light irradiation.

MATERIALS AND METHODS

Preparation of Mesoporous WO_3

All chemicals used were of analytical grade. A series of mesoporous WO_3 were synthesized via the EISA process using WCl_6 as a precursor and diblock copolymers PEO_x-b-PS_y as templates, which was similar to a previous work (Zhu et al., 2017). Typically, 0.1 g templates were dissolved into 5.0 g tetrahydrofuran (THF) to form solution A. Solution B was then prepared by adding 0.25 g WCl_6 into a mixed solution of 0.5 g ethanol and 0.25 g acetylacetone (AcAc). Solutions A and B were subsequently mixed under stirring for 2 h at room temperature. The obtained solution mentioned above was then placed in Petri dishes to evaporate the solvent at room temperature for 1 h and heated at 100°C for 24 h. Finally, the resulting transparent films were further calcined at 350°C in N_2 for 3 h and then 500°C in air for 2 h at a heating rate of 1°C/min.

Preparation of Samples

A one-step hydrothermal method was employed to synthesize the N,Cu-CDs. Typically, 0.68 mmol folic acid (FA) and 0.13 mmol copper nitrate trihydrate ($Cu(NO_3)_2{\cdot}3H_2O$) were dissolved into 30 ml of deionized water under stirring for 20 min at room temperature. Afterward, the solution was transferred to a 100 ml Teflon-lined autoclave that was placed in an oven at 200°C for 4 h. Finally, the CDs solution mentioned above was filtered using 0.22 μm filtration membranes and dialyzed by using a 1000 Da dialysis bag for 8 h. The CD powders were then obtained by a freeze-dry process.

A sonication-assisted hydrothermal method was employed to synthesize the nanocomposites. Typically, 0.1 g of m-WO_3 was added into different CD solution concentrations (0.2–1.0 g/L, 20 ml) followed by sonication for 15 min to expel any pore resident bubbles to form a homogeneous suspension. Subsequently, the suspension was poured into a Teflon-lined autoclave (50 ml) and heated at 190°C for 8 h. Finally, the precipitates were obtained by centrifugation at 8000 r/min and dried in an oven at 70°C. A series of N,Cu-CDs/m-WO_3 nanocomposites were synthesized and designated as N,Cu-CD/m-WO_3-C (C = 0.2–1.0). The N-CDs/m-WO_3 nanocomposites were obtained by the same method, except for the N-CDs prepared in our previous work (Ni et al., 2020).

Measurements

Scanning electron microscopy (SEM) and transmission electron microscopy (TEM) tests were performed with Quanta FEG 450 and Tecnai G220S-Twin microscopes, respectively. X-ray diffraction (XRD) measurements were obtained using a Bruker D8 Advance X-ray diffractometer. X-ray photoelectron spectroscopy (XPS) was characterized by using the EscaLab 250Xi spectrometer. The UV–vis–NIR diffuse reflection spectra (DRS) were analyzed with a Shimadzu UV2600 spectrophotometer. Fourier-transform infrared (FT-IR) and photoluminescence (PL) spectra were investigated using Shimadzu IRTracer-100 and Edinburgh FLS1000 spectrometers, respectively. Nitrogen adsorption–desorption isotherms were measured with an Autosorb IQ analyzer. A Malvern Nano ZS laser particle-size analyzer was employed to investigate the particle diameters.

Photodegradation Experiments

A 300 W high-pressure mercury lamp (λ = 365 nm, the average light intensity was 50 $mW{\cdot}cm^{-2}$), 500 W gold halide lamp

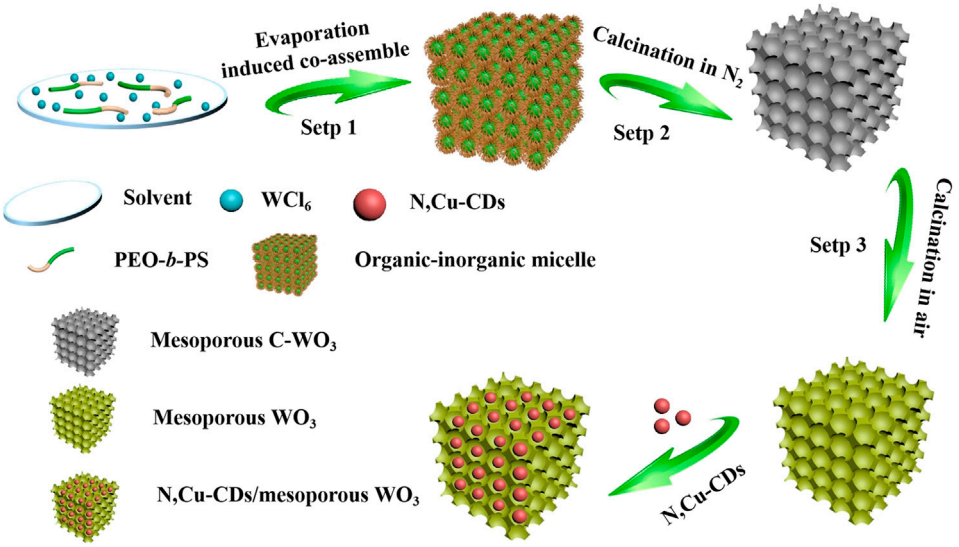

SCHEME 1 | The formation process of the ordered N, Cu-CDs/m-WO_3 composite.

($\lambda \geq 420$ nm, the average light intensity was 30 mW·cm^{-2}), and 500 W xenon lamp ($\lambda \geq 780$ nm, the average light intensity was 25 mW·cm^{-2}) were employed to provide UV, visible, and NIR light, respectively. For each experiment, 50 ml of RhB (10 mg/L), MB (10 mg/L), CIP (20 mg/L), OTC (20 mg/L), BPA (20 mg/L), and TCH (20 mg/L) solutions containing 50 mg of the photocatalysts were stirred in the dark for 30 min to achieve adsorption–desorption equilibrium. The reaction conditions were controlled at 25 ± 1°C. The concentrations of RhB and MB were detected using a UV-2600 spectrophotometer. The concentrations of CIP, OTC, BPA, and TCH were analyzed by high-performance liquid chromatography (see *Supplementary Material*).

Photoelectrochemical Tests

The PEC properties including the photocurrent response and electrochemical impedance spectroscopy (EIS) were performed on an electrochemical workstation (Princeton, VersaSTAT 3) with Na_2SO_4 (0.5 M) solution as the electrolyte. The as-synthesized samples, a Pt plate, and a saturated calomel electrode (SCE) electrode were employed as the working electrode, counter electrode, and reference electrode, respectively. The working electrode was prepared on FTO glass via a spin-coating method, and a 300 W xenon lamp was used to simulate the solar light.

RESULTS AND DISCUSSION

The Synthesis Route for the N,Cu-CDs/M-WO_3 Nanocomposite

As shown in **Scheme 1**, the WCl_6 and PEO_x-b-PS_y were chosen as the precursor and template, respectively. The m-WO_3 with a large specific surface area and highly ordered pore sizes was successfully synthesized via an EISA process and then calcining under an N_2 and air atmosphere. The N,Cu-CDs were prepared by a facile one-step hydrothermal method, using folic acid and copper nitrate hydrate as C and Cu sources. A sonication-assisted hydrothermal approach was used to synthesize the N,Cu-CDs/m-WO_3 nanocomposite, in which the N,Cu-CDs were well located at the pores of the m-WO_3.

Micromorphology Analysis

The SEM and TEM images (**Figures 1A–C**) indicate that the m-WO_3 possessed highly ordered and uniform pores with dimensions of ~30 nm, which was in good accordance with the pore size of the Barrett–Joyner–Halenda (BJH) results. Moreover, the hollow pores could significantly enhance its multiple light-reflection capacities. N,Cu-CDs with average sizes of 3.2 nm could be easily found within the pores (**Figures 1D,E**). The HRTEM patterns shown in **Figure 1F** reveal that the m-WO_3 exhibited a good crystalline structure with a lattice spacing of 0.365 nm, which corresponded well to the (200) lattice plane of WO_3 (Zhu et al., 2017). In addition, the N,Cu-CDs showed a lattice distance of 0.22 nm.

Brunner–Emmet–Teller and BJH Analysis

As shown in **Figure 2**, compared to the BET results of the three mesoporous WO_3 samples, the m-WO_3 with PEO_x-b-PS_y as the template possessed the largest specific surface area of 35.350 m^2/g, which was much higher than that of commercial WO_3 (6.135 m^2/g). After coupling the N,Cu-CDs and N-CDs, the specific surface area of m-WO_3 was reduced to 29.431 m^2/g and 22.465 m^2/g, respectively. Furthermore, the average pore size decreased from 30.566 to 17.083 nm and 17.361 nm within the pores (shown in **Figure 2**).

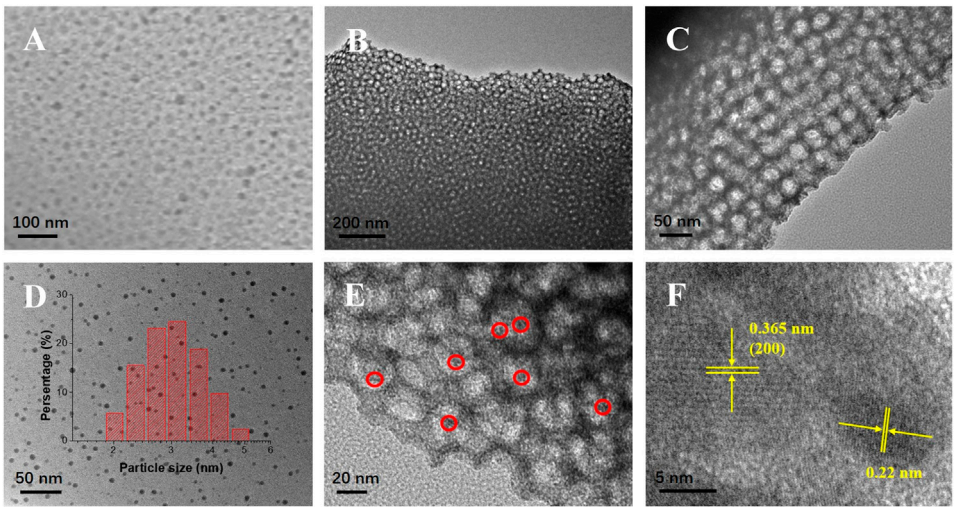

FIGURE 1 | SEM and TEM images of as-synthesized samples. SEM image of N,Cu-CDs/m-WO_3 **(A)**; TEM images of N,Cu-CDs/m-WO_3 **(B)** and **(C)**; TEM image of N,Cu-CDs **(D)**; and FETEM images of N,Cu-CDs/m-WO_3 **(E–F)**.

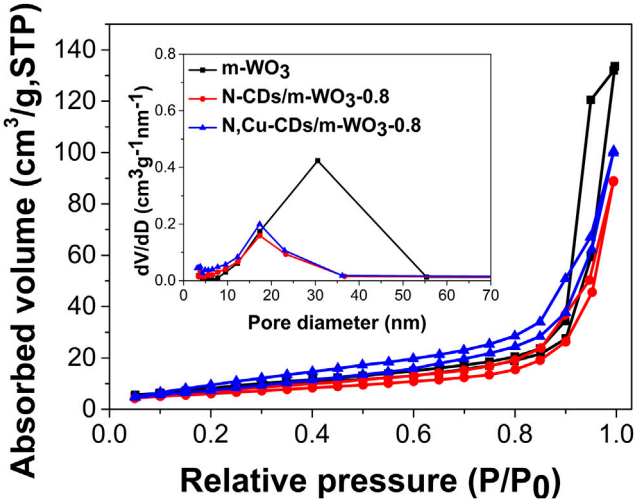

FIGURE 2 | The nitrogen adsorption–desorption isotherms of the as-synthesized samples. Inset depicts the BJH pore-size distributions.

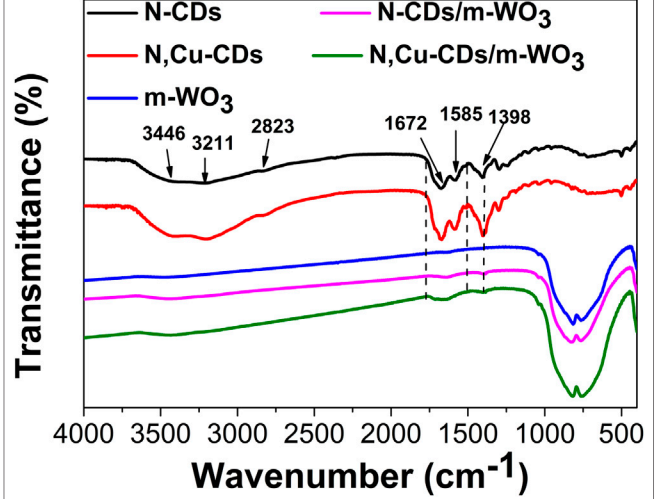

FIGURE 3 | FT-IR spectra of the as-synthesized samples.

Chemical Group Analysis

Figure 3 shows the FT-IR spectra of the N-CDs and N,Cu-CDs. The bands at 3446 cm^{-1}, 3211 cm^{-1}, 2823 cm^{-1}, 1672 cm^{-1}, 1585 cm^{-1}, and 1398 cm^{-1} were ascribed to the v (O-H), v (N-H), v (C-H), v (C=O), δ (N-H), and v (C-O), respectively. There was no obvious band for Cu due to its low content. Compared with pure m-WO_3, the expanded regions between 1750 and 1500 cm^{-1}, as well as the bands at 1398 cm^{-1} (v (C-O)) in the m-WO_3/N-CD and N,Cu-CDs/m-WO_3 nanocomposites, confirmed the successful introduction of the CDs (Zhang et al., 2017; Zhang J. et al., 2019; Ni et al., 2020). In addition, the bands between 1000 cm^{-1} and 500 cm^{-1} were assigned to the vibration of W-O-W (Zhan et al., 2018).

Crystal Structure and Element Analysis

The XRD patterns of as-prepared samples (**Figure 4A**) revealed obvious diffraction peaks at 23.1°, 23.5°, 24.4°, 33.4°, 39.9°, and 49.8°, corresponding to the (002), (020), (200), (022), (202), and (140) planes of WO_3, indicating that the m-WO_3 belonged to the monoclinic WO_3 (JCPDS No. 43-1035) (Zhu et al., 2017; Ma G. et al., 2017). There was no obvious change in the diffraction peaks of N-CDs/m-WO_3-0.8 and N,Cu-CDs/m-WO_3-0.8, which suggested that the CDs did not alter the phase structure of m-WO_3.

XPS measurements were employed to analyze the states of elements. In the survey scan of the XPS spectra of the N,Cu-CDs/m-WO_3-0.8 nanocomposite (**Supplementary Figure S1**), the presence of C, N, O, W, and Cu further verified that the

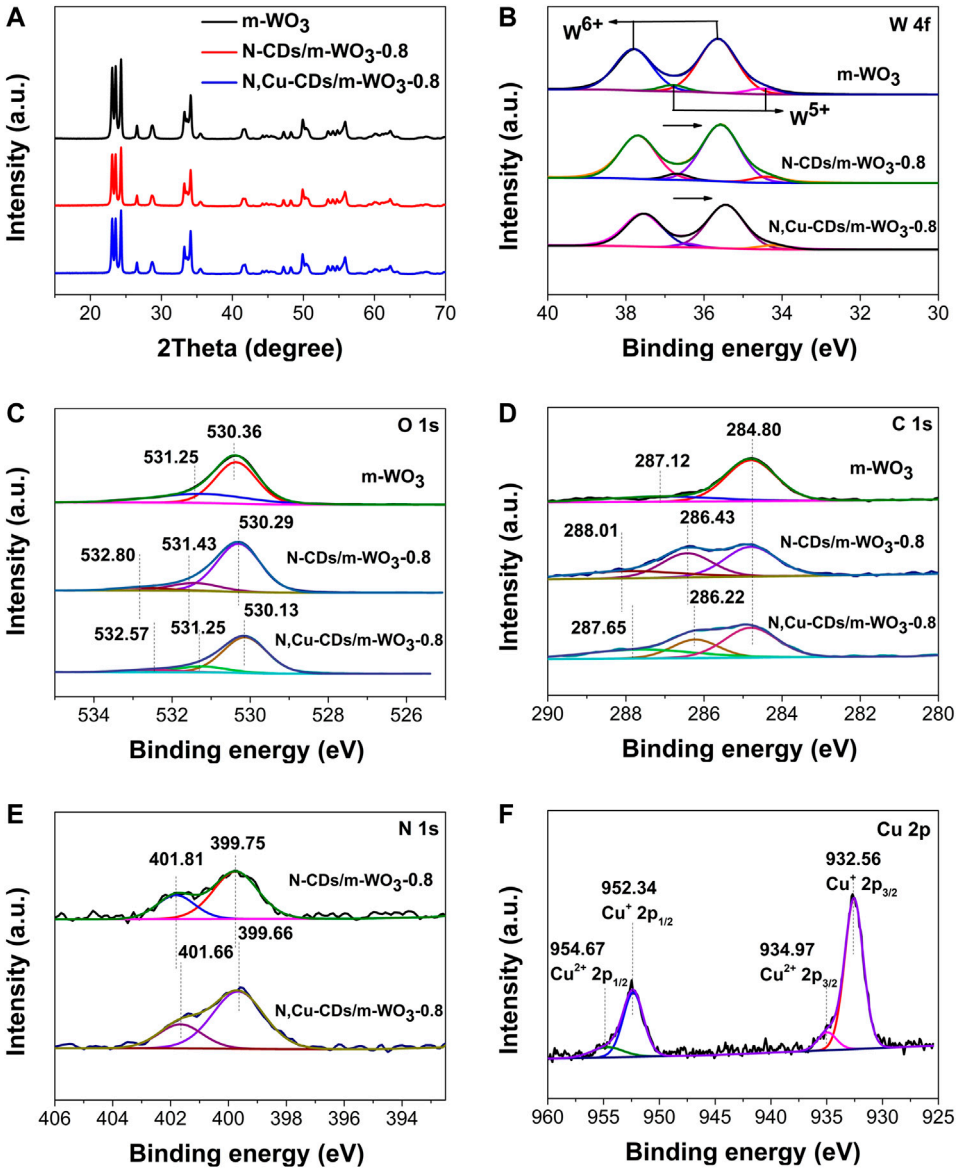

FIGURE 4 | XRD and XPS spectra of the as-synthesized samples. XRD **(A)**; W 4f **(B)**; O 1s **(C)**; C 1s **(D)**; N 1s **(E)**; and Cu 2p **(F)**.

N,Cu-CDs were successfully combined with the m-WO_3. In the high-resolution W 4f spectra (**Figure 4B**), the W of pure m-WO_3 existed in four different states: W $4f_{5/2}$ of W^{6+}, W $4f_{7/2}$ of W^{6+}, W $4f_{5/2}$ of W^{5+}, and W $4f_{7/2}$ of W^{5+} (at 37.80, 35.64, 36.80, and 34.50 eV, respectively), which suggested that the m-WO_3 contained rich oxygen vacancies (Sun et al., 2019). In the O 1s spectra (**Figure 4C**), the O 1s peaks in the pure m-WO_3 were divided into two peaks at 530.36 and 531.25 eV, which were ascribed to the lattice oxygen (W-O) and the adsorbed oxygen, respectively (Zhu et al., 2017). As for the O 1s of N-CDs/m-WO_3 and N,Cu-CDs/m-WO_3-0.8, the new peaks appearing at ~533 eV belonged to the binding energy of C=O in the CDs. It can be clearly observed that the W4f and O 1s peaks of the nanocomposites showed shifts to lower binding energies after decorating with N-CDs or N,Cu-CDs, which was due to the interactions between the CDs and m-WO_3 (Di et al., 2015). Moreover, the introduction of Cu could further enhance this effect.

As shown in the C 1s spectra (**Figure 4D**), the peaks at 284.80 and 287.12 eV in the pure m-WO_3 were attributed to the surface carbon from ambient air (Ni et al., 2020). After decorating with N,Cu-CDs, the new C 1s peaks appearing at 287.65 and 286.22 eV were attributed to the C=O, C–O/C–N bands of the CDs, respectively (Peng et al., 2019; Zhang J. et al., 2019). According to the N 1s spectra of the N,Cu-CDs/m-WO_3-0.8 nanocomposite (**Figure 4E**), the peaks at ~399.66 and 401.66 eV were assigned to C-N and N-H bonds, respectively (Yang et al., 2018). Compared with the N-CD-decorated m-WO_3, the C 1s

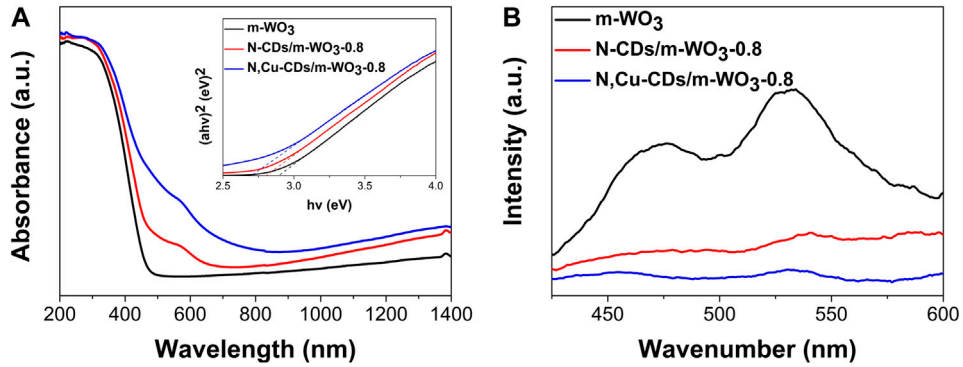

FIGURE 5 | UV–vis–NIR diffuse reflectance spectra (DRS) and band-gap analysis **(A)**; photoluminescence (PL) spectra of the as-synthesized samples **(B)**.

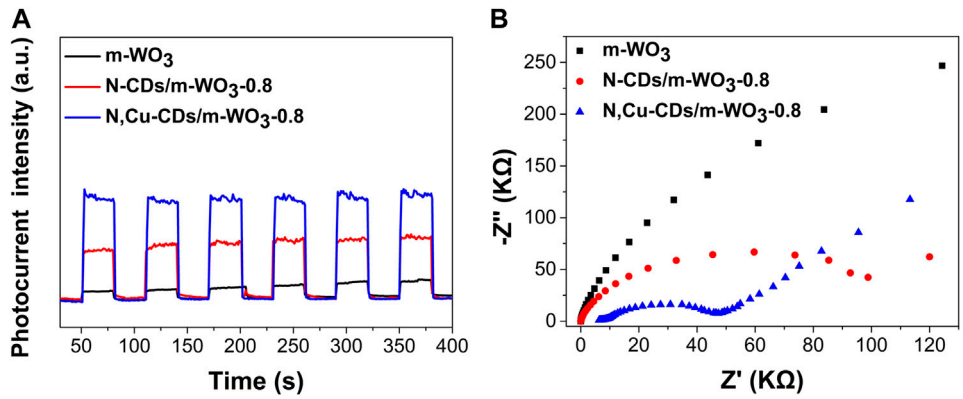

FIGURE 6 | PEC properties of as-synthesized samples: photocurrent response **(A)** and EIS measurement **(B)**.

and N 1s peaks in the N,Cu-CDs/m-WO_3-0.8 nanocomposite underwent shifts, which was caused by the chelation between the Cu and N-CDs (Orozco-Guareño et al., 2010). In addition, as shown in the Cu 2p spectra of the N,Cu-CDs/m-WO_3-0.8 (**Figure 4F**), the Cu components with their Cu $2p_{3/2}$ and Cu $2p_{1/2}$ binding energies at 932.56 and 952.34 eV were characteristic of Cu^{1+}, while the shoulder peaks at 934.97 eV for Cu $2p_{3/2}$ and 954.67 eV for Cu $2p_{1/2}$ could be ascribed to Cu^{2+} (Orozco-Guareño et al., 2010; Liu et al., 2015; and Li et al., 2014). The transformable valence states of Cu demonstrated that the N,Cu-CDs could serve as multielectron redox reaction sites for the efficient electron migration.

Optical Property Analysis

Figure 5A shows the UV–vis–NIR absorption in the regions of 200–1400 nm with the inset for band gaps. Interestingly, beyond the intrinsic absorption edge of 480 nm, pure m-WO_3 showed the absorption ability in the NIR region, which could be attributed to the existence of oxygen vacancies (Liu L. et al., 2012; Wu et al., 2019) and multiple light-reflection within the pores (Yan et al., 2019; Ni et al., 2020). Compared to the pure m-WO_3, the N-CD- and N,Cu-CD-decorated m-WO_3 performed the reduced band gaps (m-WO_3) from 2.9 to 2.8 eV and 2.7 eV, respectively. In particular, the N,Cu-CDs/m-WO_3-0.8 nanocomposite exhibited a broader optical absorption from the UV to NIR regions, suggesting that more solar energy could be utilized through N,Cu-CDs decorating.

As shown in **Figure 5B**, the N,Cu-CD-decorated m-WO_3 showed a significantly decreased PL intensity, indicating the efficient electron transfer capacity of N,Cu-CDs/m-WO_3-0.8, which could greatly accelerate the separation of e^-/h^+ pairs (Liang et al., 2017).

PEC Properties

The photocurrent response and EIS tests were conducted to further investigate the migration and separation of photoinduced electrons and holes. As shown in **Figure 6A**, the N,Cu-CDs/m-WO_3-0.8 nanocomposite showed the highest photocurrent intensity in contrast to the pure m-WO_3 and the N-CDs/m-WO_3-0.8 under solar light irradiation, suggesting faster electron transfer and highly efficient separation of e^-/h^+ pairs in the N,Cu-CDs/m-WO_3-0.8. In the EIS spectrum (**Figure 6B**), a smaller semicircle arc radius implied a smaller resistance at the interfacial region, which further demonstrated

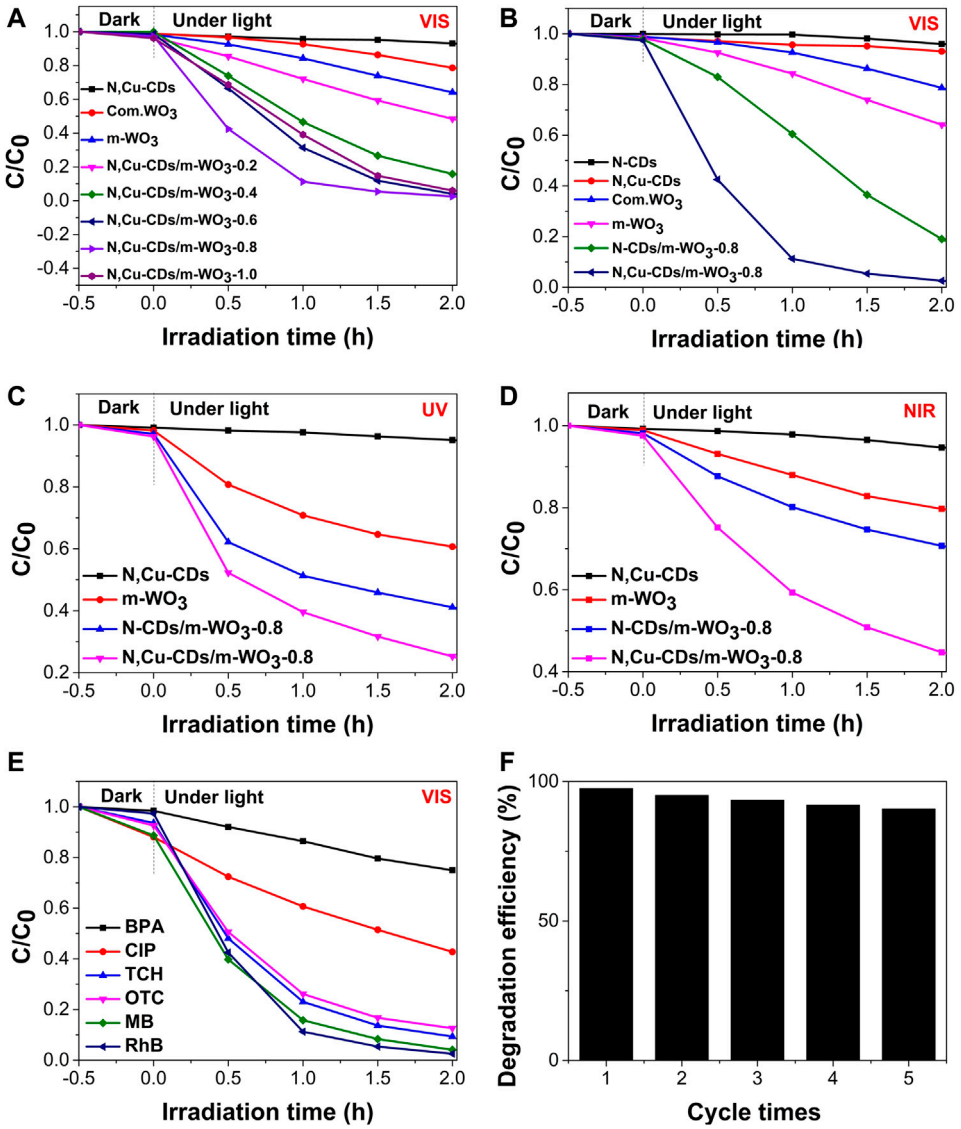

FIGURE 7 | Photocatalytic performance of as-synthesized samples under UV, vis, and NIR light irradiation. **(A)** The photocatalytic efficiencies of m-WO_3 decorated with different amount of N,Cu-CDs under visible light irradiation; **(B–D)** were the comparasion of photocatalytic activities under UV, vis, and NIR light irradiation, respectively; **(E)** The photocatalytic efficiencies on various pollutants over N,Cu-CDs/m-WO_3-0.8 under visible light irradiation; **(E)** The photocatalytic stability of N,Cu-CDs/m-WO_3-0.8.

that the N,Cu-CDs/m-WO_3-0.8 nanocomposite possessed faster interfacial charge transfer and a lower e^-/h^+ pair recombination rate compared with m-WO_3 (Zhang et al., 2017; Zhang J. et al., 2019).

Photocatalytic Performance

As shown in **Figure 7A**, among the m-WO_3 with different contents of N,Cu-CDs, the N,Cu-CDs/m-WO_3-0.8 nanocomposite showed the highest photodegradation efficiency on RhB under visible-light irradiation. Compared with the pure m-WO_3 and N-CDs/m-WO_3-0.8 nanocomposite, the N,Cu-CDs/m-WO_3-0.8 nanocomposite exhibited higher photodegradation efficiencies of 81.5, 97.6, and 56.2%, respectively, after 2 h of UV–vis–NIR light irradiation (**Figures 7B–D**), respectively. Furthermore, the kinetics of the RhB photodegradation was investigated. As displayed in **Supplementary Figure S2**, the highest photodegradation rate constant of 1.895 h^{-1} under visible light irradiation was found by the N,Cu-CDs/m-WO_3-0.8 nanocomposite, whereas the photodegradation rate of commercial WO_3 was only 0.083 h^-. This suggests that the photodegradation rate of N,Cu-CDs/m-WO_3-0.8 was almost 23 times higher than that of commercial WO_3. In addition, the N,Cu-CDs/m-WO_3-0.8 nanocomposite showed excellent photocatalytic performance for the degradation of MB, TCH, OTC, CIP, and BPA under visible-light irradiation for 2 h

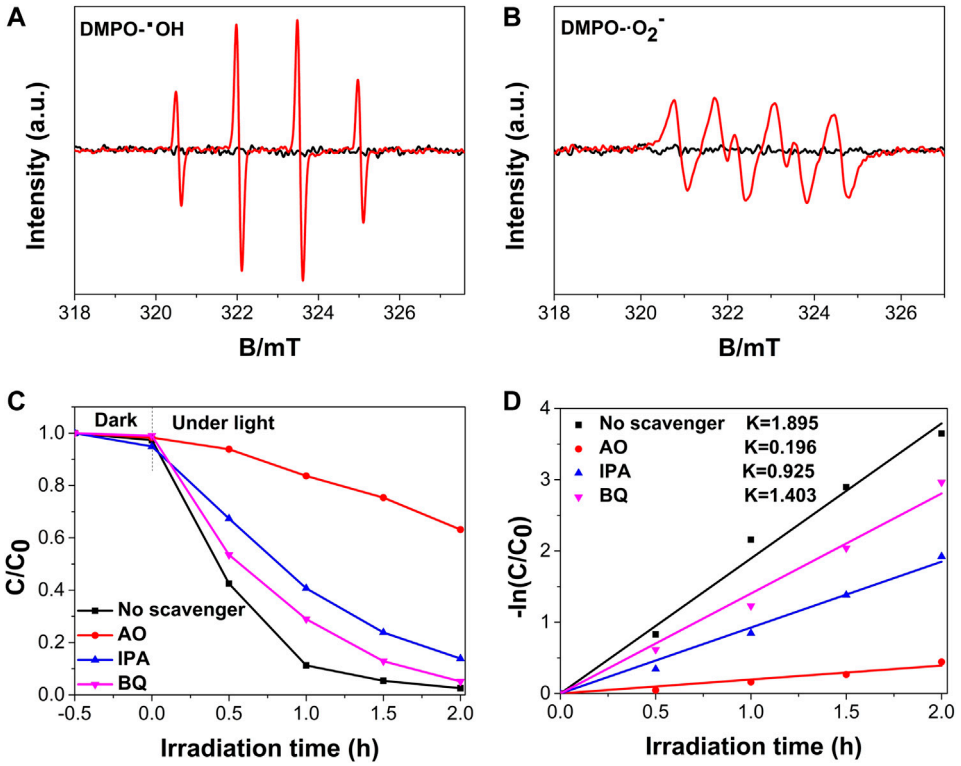

FIGURE 8 | DMPO ESR and ROSs trapping experiments of the N,Cu-CDs/m-WO_3-0.8 nanocomposite: DMPO-·OH **(A)**; DMPO-·O2- **(B)**; ROSs trapping experiments **(C)**; and kinetic fit for ROSs trapping experiments **(D)**.

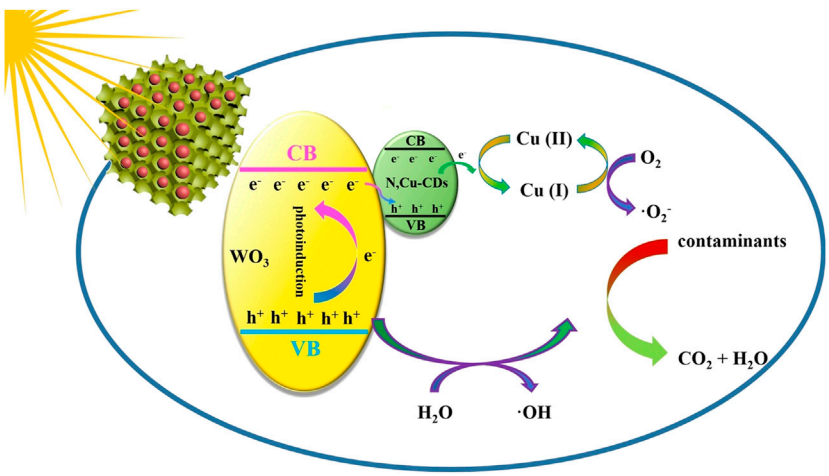

FIGURE 9 | Photocatalytic mechanism of the N,Cu-CDs/m-WO_3-0.8 nanocomposite.

(**Figure 7E**). The stability of the N,Cu-CDs/m-WO_3-0.8 nanocomposite was studied via the cycling tests under visible-light irradiation for 2 h. **Figure 7F** shows that the nanocomposite maintained almost unchanged RhB photodegradation efficiencies varying from 97.6 to 90.2% after a five-cycle recycling, confirming the stable and reusable properties of the N,Cu-CDs/m-WO_3-0.8 nanocomposite.

Photocatalytic Mechanism

Electron spin resonance (ESR) tests using DMSO were conducted to investigate the reactive oxygen species (ROSs) in the N,Cu-CDs/m-WO_3-0.8 nanocomposite under solar light irradiation. As shown in **Figures 8A,B**, four peaks with an intensity ratio of 1: 2:2:1 corresponded to the signal of DMPO-·OH, and the characteristic peaks of DMPO-·O_2^-- could be clearly observed

(Xiao et al., 2018). Moreover, the signal intensity of DMPO-·OH was significantly stronger than that of DMPO-·O_2^-, suggesting that ·OH might be the primary reactive species in the photoreaction. To further examine the key reactive species in the N,Cu-CDs/m-WO_3-0.8 composite, ROSs trapping experiments were conducted by adding various scavengers including AO (700 mg/L) for h^+, IPA (600 mg/L) for ·OH, and BQ (80 mg/L) for ·O_2^- (Cai et al., 2019). As presented in **Figures 8C,D**, the photodegradation rate of RhB showed partial inhibition rates of 89.67, 51.19, and 25.95% after adding the scavengers of AO, IPA, and BQ, respectively, indicating that the photogenerated h^+ and OH were the main ROSs in the photocatalytic reaction.

Based on the abovementioned results, a possible photocatalytic mechanism for the N,Cu-CDs/m-WO_3-0.8 nanocomposite was proposed as follows (**Figure 9**). Under UV–vis–NIR light irradiation, both m-WO_3 and N,Cu-CDs were excited, thus forming the e^-/h^+ pairs. The photoinduced electrons in the conduction band (CB) of m-WO_3 combined with the h^+ in the valence band (VB) of the N,Cu-CDs. Moreover, the photoinduced e^- was directly transferred from the VB of the N,Cu-CDs to Cu(II), forming a multielectron reaction site, where Cu(II) was reduced to Cu(I). Subsequently, Cu(I) was oxidized to Cu(II) with the conversion of O_2 to ·O_2^- (Irie et al., 2008; Ma et al., 2018), whereas the remaining h^+ in the VB of m-WO_3 could directly photodegrade the contaminants or indirectly transfer H_2O to ·OH (Wang et al., 2019; Ni et al., 2020). Therefore, the introduction of N,Cu-CDs as multielectron reaction sites could greatly accelerate electron transfer and efficiently prevent the recombination of e^-/h^+ pairs.

CONCLUSION

In summary, mesoporous WO_3 with a large specific surface area was successfully synthesized via the EISA process with PbS as the template. For the first time, the N,Cu-CDs/m-WO_3-0.8 nanocomposite was prepared by a sonication-assisted hydrothermal method. The N,Cu-CDs/m-WO_3-0.8 nanocomposite, with a large specific surface area, full-spectrum response, efficient electron-transfer capacity, and low e^-/h^+ pair recombination rate, exhibited outstanding photocatalytic activities for the degradation of RhB, MB, TCH, OTC, CIP, and BPA. Characterization results demonstrate that the conversion between Cu (II) and Cu (I) played a key role in accelerating electron transfer and inhibiting the recombination of e^-/h^+ pairs. Furthermore, the extended spectrum absorption was attributed to the ample oxygen vacancies, the introduction of N,Cu-CDs, and multiple light reflections within the pores of the mesoporous WO_3.

DATA AVAILABILITY STATEMENT

The original contributions presented in the study are included in the article/**Supplementary Material**; further inquiries can be directed to the corresponding authors.

AUTHOR CONTRIBUTIONS

TN and KC conceptualized the work; TN and QL curated data; QL conducted formal analysis; ZY acquired fund; TN, YY, KC, and GL conducted investigation; YY was responsible for the methodology; TN, ZY, and GL supervised the work; TN and QL wrote the original draft; and TN and GL reviewed and edited the manuscript.

FUNDING

This work was supported by the National Natural Science Foundation of China (No. 21677040).

SUPPLEMENTARY MATERIAL

The Supplementary Material for this article can be found online at: https://www.frontiersin.org/articles/10.3389/fmats.2021.649411/full#supplementary-material.

REFERENCES

Barman, M. K., Jana, B., Bhattacharyya, S., and Patra, A. (2014). Photophysical properties of doped carbon dots (N, P, and B) and their influence on electron/hole transfer in carbon dots–nickel (II) phthalocyanine conjugates. *J. Phys. Chem. C* 118, 20034–20041. doi:10.1021/jp507080c

Cai, Z., Hao, X., Sun, X., Du, P., Liu, W., and Fu, J. (2019). Highly active WO_3 @anatase-SiO_2 aerogel for solar-light-driven phenanthrene degradation: mechanism insight and toxicity assessment. *Water Res.* 162, 369–382. doi:10.1016/j.watres.2019.06.017

Carmona, R. J., Velasco, L. F., Laurenti, E., Maurino, V., and Ania, C. O. (2016). Carbon materials as additives to WO_3 for an enhanced conversion of simulated solar light. *Front. Mater.* 3, 9. doi:10.3389/fmats.2016.00009

Daneshvar, N., Khataee, A. R., Rasoulifard, M. H., and Pourhassan, M. (2007). Biodegradation of dye solution containing malachite green: optimization of effective parameters using Taguchi method. *J. Hazard. Mater.* 143, 214–219. doi:10.1016/j.jhazmat.2006.09.016

Di, J., Xia, J., Ge, Y., Li, H., Ji, H., Xu, H., et al. (2015). Novel visible-light-driven CQDs/Bi_2WO_6 hybrid materials with enhanced photocatalytic activity toward organic pollutants degradation and mechanism insight. *Appl. Catal. B* 168–169, 51–61. doi:10.1016/j.apcatb.2014.11.057

Guo, Y., Zhang, L., Zhang, S., Yang, Y., Chen, X., and Zhang, M. (2015). Fluorescent carbon nanoparticles for the fluorescent detection of metal ions. *Biosens. Bioelectron.* 63, 61–71. doi:10.1016/j.bios.2014.07.0110.1016/j.bios.2014.07.018

Irie, H., Miura, S., Kamiya, K., and Hashimoto, K. (2008). Efficient visible light-sensitive photocatalysts: grafting Cu(II) ions onto TiO_2 and WO_3 photocatalysts. *Chem. Phys. Lett.* 457, 202–205. doi:10.1016/j.cplett.2008.04.006

Li, H., Kang, Z., Liu, Y., and Lee, S. (2012). Carbon nanodots: synthesis, properties and applications. *J. Mater. Chem.* 22, 24230–24253. doi:10.1039/c2jm34690g

Li, L., Krissanasaeranee, M., Pattinson, W. S., Stefik, M., Wiesner, U., Steiner, U., et al. (2010). Enhanced photocatalytic properties in well-ordered mesoporous WO_3. *Chem. Commun.* 46, 7620–7622. doi:10.1039/c0cc01237h

Li, Z. P., Wen, Y. Q., Shang, J. P., Wu, M. X., Wang, L. F., and Guo, Y. (2014). Magnetically recoverable Cu_2O/Fe_3O_4 composite photocatalysts: fabrication and photocatalytic activity. *Chin. Chem. Lett.* 25, 287–291. doi:10.1016/j.cclet.2013.10.023

Liang, Z., Wei, J., Wang, X., Yu, Y., and Xiao, F. (2017). Elegant Z-scheme-dictated g-C_3N_4 enwrapped WO_3 superstructures: a multifarious platform for versatile photoredox catalysis. *J. Mater. Chem. A* 5, 15601–15612. doi:10.1039/c7ta04333c

Liu, L., Zhang, Y., Wang, A., and Zhang, T. (2012). Mesoporous WO_3 supported Pt catalyst for hydrogenolysis of glycerol to 1,3-propanediol. *Chin. J. Catal.* 33, 1257–1261. doi:10.1016/S1872-2067(11)60425-7

Liu, Y., Ya, Y., Li, W., Han, S., and Liu, C. (2012). Photoelectrochemical properties and photocatalytic activity of nitrogen-doped nanoporous WO_3 photoelectrodes under visible light. *Appl. Surf. Sci.* 258, 5038–5045. doi:10.1016/j.apsusc.2012.01.080

Liu, Y., Zhang, B., Luo, L., Chen, X., Wang, Z., Wu, E., et al. (2015). TiO_2/Cu_2O core/ultrathin shell nanorods as efficient and stable photocatalysts for water reduction. *Angew. Chem. Int. Ed.* 54, 15260–15265. doi:10.1002/ange.201509115 10.1002/anie.201509115

Luo, W., Li, Y., Dong, J., Wei, J., Xu, J., Deng, Y., et al. (2013). A resol-assisted co-assembly approach to crystalline mesoporous niobia spheres for electrochemical biosensing. *Angew. Chem. Int. Ed.* 125, 10699–10704. doi:10.1002/ange.201303353

Lv, Y., Xu, Z., Irie, S., and Nakane, K. (2017). Fabrication of PdO_x loaded highly mesoporous WO_3/TiO_2 hybrid nanofibers by stepwise pore-generation for enhanced photocatalytic performance. *Mol. Catal.* 438, 173–183. doi:10.1016/j.mcat.2017.05.024

Ma, G., Chen, Z., Chen, Z., Jin, M., Meng, Q., Yuan, M., et al. (2017). Constructing novel WO_3/Fe(III) nanofibers photocatalysts with enhanced visible-light-driven photocatalytic activity via interfacial charge transfer effect. *Mater. Today* 3, 45–52. doi:10.1016/j.mtener.2017.02.003

Ma, G., Lu, J., Meng, Q., Lv, H., Shuai, L., Zhang, Y., et al. (2018). Synergistic effect of Cu-ion and WO_3 nanofibers on the enhanced photocatalytic degradation of rhodamine B and aniline solution. *Appl. Surf. Sci.* 451, 306–314. doi:10.1016/j.apsusc.2018.04.236

Ma, Y., Cen, Y., Sohail, M., Xu, G., Wei, F., Shi, M., et al. (2017). A ratiometric fluorescence universal platform based on N, Cu codoped carbon dots to detect metabolites participating in H_2O_2-generation reactions. *ACS Appl. Mater. Inter.* 9, 38. doi:10.1021/acsami.7b10548

Nakajima, T., Kitamura, T., and Tsuchiya, T. (2011). Visible light photocatalytic activity enhancement for water purification in Cu(II)-grafted WO_3 thin films grown by photoreaction of nanoparticles. *Appl. Catal. B* 108–109, 47–53. doi:10.1016/j.apcatb.2011.08.006

Ni, T., Li, Q., Yan, Y., Wang, F., Cui, X., Yang, Z., et al. (2020). N,Fe-Doped carbon dot decorated gear-shaped WO_3 for highly efficient UV-Vis-NIR-Driven photocatalytic performance. *Catalysts* 10, 416. doi:10.3390/catal10040416

Ong, W.-J. (2017). 2D/2D graphitic carbon nitride (g-C_3N_4) heterojunction nanocomposites for photocatalysis: why does face-to-face interface matter?. *Front. Mater.* 4, 11. doi:10.3389/fmats.2017.00011

Orozco-Guareño, E., Santiago-Gutiérrez, F., Morán-Quiroz, J. L., Hernandez-Olmos, S. L., Soto, V., Cruz, W., et al. (2010). Removal of Cu(II) ions from aqueous streams using poly(acrylic acid-co-acrylamide) hydrogels. *J. Colloid Interf. Sci.* 349, 583–593. doi:10.1016/j.jcis.2010.05.048

Peng, H., Liu, D., Zheng, X., and Fu, X. (2019). N-doped carbon-coated ZnS with sulfur-vacancy defect for enhanced photocatalytic activity in the visible light region. *Nanomaterials* 9, 1657. doi:10.3390/nano9121657

Sun, J., Sun, L., Han, N., Pan, J., Liu, W., Bai, S., et al. (2019). Ordered mesoporous WO_3/ZnO nanocomposites with isotype heterojunctions for sensitive detection of NO_2. *Sens. Actuators B* 285, 68–75. doi:10.1016/j.snb.2018.12.089

Teoh, L. G., Hon, Y. M., Shieh, J., Lai, W. H., and Hon, M. H. (2003). Sensitivity properties of a novel NO_2 gas sensor based on mesoporous WO_3 thin film. *Sens. Actuators B* 96, 219–225. doi:10.1016/S0925-4005(03)00528-8

Wang, F., Chen, P., Feng, Y., Xie, Z., Liu, Y., Su, Y., et al. (2017). Facile synthesis of N-doped carbon dots/g-C_3N_4 photocatalyst with enhanced visible-light photocatalytic activity for the degradation of indomethacin. *Appl. Catal. B* 207, 103–113. doi:10.1016/j.apcatb.2017.02.024

Wang, F., Wu, Y., Wang, Y., Li, J., Jin, X., Zhang, Q., et al. (2019). Construction of novel Z-scheme nitrogen-doped carbon dots/{0 0 1} TiO_2 nanosheet photocatalysts for broad-spectrum-driven diclofenac degradation: mechanism insight, products and effects of natural water matrices. *Chem. Eng. J.* 356, 857–868. doi:10.1016/j.cej.2018.09.092

Wang, S., Fan, W., Liu, Z., Yu, A., and Jiang, X. (2018). Advances on tungsten oxide based photochromic materials: strategies to improve photochromic properties. *J. Mater. Chem. C* 6, 191–212. doi:10.1039/C7TC04189F

Wu, C.-M., Naseem, S., Chou, M.-H., Wang, J.-H., and Jian, Y.-Q. (2019). Recent advances in tungsten-oxide-based materials and their applications. *Front. Mater.* 6, 49. doi:10.3389/fmats.2019.00049

Wu, W., Zhan, L., Fan, W., Song, J., Li, X., Li, Z., et al. (2015). Cu-N dopants boost electron transfer and photooxidation reactions of carbon dots. *Angew. Chem. Int. Ed.* 54, 6540–6544. doi:10.1002/anie.201501912

Wu, Z. L., Liu, Z. X., and Yuan, Y. H. (2017). Carbon dots: materials, synthesis, properties and approaches to long-wavelength and multicolor emission. *J. Mater. Chem. B* 5, 3794–3809. doi:10.1039/c7tb00363c

Xiao, T., Tang, Z., Yang, Y., Tang, L., Zhou, Y., and Zou, Z. (2018). *In situ* construction of hierarchical WO_3/g-C_3N_4 composite hollow microspheres as a Z-scheme photocatalyst for the degradation of antibiotics. *Appl. Catal. B* 220, 417–428. doi:10.1016/j.apcatb.2017.08.070

Xu, P., Wang, C., Sun, D., Chen, Y., and Zhuo, K. (2015). Ionic liquid as a precursor to synthesize nitrogen- and sulfur-co-doped carbon dots for detection of copper(II) ions. *Chem. Res. Chin. Univ.* 31, 730–735. doi:10.1007/s40242-015-5118-y

Xue, N., Kong, X., Song, B., Bai, L., Zhao, Y., Lu, C., et al. (2017). Cu-doped carbon dots with highly ordered alignment in anisotropic nano-space for improving the photocatalytic performance. *Sol. RRL* 1, 1700029. doi:10.1002/solr.201700029

Yan, Y., Chang, K., Ni, T., and Li, K. (2019). L-cysteine assisted synthesis of Bi_2S_3 hollow sphere with enhanced near-infrared light harvesting for photothermal conversion and drug delivery. *Mater. Lett.* 245, 158–161. doi:10.1016/j.matlet.2019.02.104

Yang, L., Liu, Y., Zhang, R., Li, W., Li, P., Wang, X., et al. (2018). Enhanced visible-light photocatalytic performance of a monolithic tungsten oxide/graphene oxide aerogel for nitric oxide oxidation. *Chin. J. Catal.* 39, 646–653. doi:10.1016/S1872-2067(17)62974-7

Zhan, Y., Liu, Y., Liu, Q., Liu, Z., Yang, H., Lei, B., et al. (2018). Size-controlled synthesis of fluorescent tungsten oxide quantum dots via one-pot ethanol-thermal strategy for ferric ions detection and bioimaging. *Sens. Actuators B* 255, 290–298. doi:10.1016/j.snb.2017.08.043

Zhang, J., Liu, J., Wang, X., Mai, J., Zhao, W., Ding, Z., et al. (2019). Construction of Z-scheme tungsten trioxide nanosheets-nitrogen-doped carbon dots composites for the enhanced photothermal synergistic catalytic oxidation of cyclohexane. *Appl. Catal. B* 259, 118063. doi:10.1016/j.apcatb.2019.118063

Zhang, J., Ma, Y., Du, Y., Jiang, H., Zhou, D., and Dong, S. (2017). Carbon nanodots/WO_3 nanorods Z-scheme composites: remarkably enhanced photocatalytic performance under broad spectrum. *Appl. Catal. B* 209, 253–264. doi:10.1016/j.apcatb.2017.03.017

Zhang, W. J., Liu, S. G., Han, L., Luo, H. Q., and Li, N. B. (2019). A ratiometric fluorescent and colorimetric dual-signal sensing platform based on N-doped carbon dots for selective and sensitive detection of copper(II) and pyrophosphate ion. *Sens. Actuators B* 283, 215–221. doi:10.1016/j.snb.2018.12.012

Zhao, T., Ren, Y., Yang, J., Wang, L., Jiang, W., Elzatahry, A. A., et al. (2016). Hierarchical ordered macro/mesoporous titania with highly interconnected porous structure for efficient photocatalysis. *J. Mater. Chem. A* 4, 16446–16453. doi:10.1039/C6TA06849A

Zheng, X., Zhang, C., Xia, J., Zhou, G., Jiang, D., Wang, S., et al. (2019). Mesoporous tungsten oxide electrodes for YSZ-based mixed potential sensors to detect NO_2 in the sub ppm-range. *Sens. Actuators B* 284, 575–581. doi:10.1016/j.snb.2019.01.016

Zhu, Y., Zhao, Y., Ma, J., Cheng, X., Xie, J., Xu, P., et al. (2017). Mesoporous tungsten oxides with crystalline framework for highly sensitive and selective detection of foodborne pathogens. *J. Am. Chem. Soc.* 139, 10365–10373. doi:10.1021/jacs.7b04221

Zong, J., Yang, X., Trinchi, A., Hardin, S., Cole, I., Zhu, Y., et al. (2014). Carbon dots as fluorescent probes for "Off-On" detection of Cu^{2+} and L-cysteine in aqueous solution. *Biosens. Bioelectron.* 51, 330–335. doi:10.1016/j.bios.2013.07.042

Conflict of Interest: The authors declare that the research was conducted in the absence of any commercial or financial relationships that could be construed as a potential conflict of interest.